Experimental study of the effect of droplets on opposed stretched premixed flames

Maxim Kuvshinov, Bertrand Lecordier, Said Idlahcen, A Cessou, Bruno Renou, Simone Hochgreb

Experimental study of the effect of droplets on opposed stretched premixed flames

M. Kuvshinov*[1], B. Lecordier[1], S. Idlahcen[1], A. Cessou[1], B. Renou[1], and S. Hochgreb[2]

[1]INSA Rouen-Normandie, UNIROUEN, CNRS, CORIA, Normandie University, Rouen 76000, France
[2]University of Cambridge, Cambridge, CB2 1PZ, United Kingdom

Abstract

The effect of fuel droplets on the burning velocity of strained laminar premixed flames was investigated experimentally using optical diagnostics. The twin counterflow burner configuration was used to create premixed acetone vapour flames with the addition of fuel droplets. Particle image velocimetry (PIV) was used to measure 2D velocities for nominal equivalence ratios in the range (0.8–1.21) as a function of strain rate (250–550 s^{-1}). Measurements of reference flame speeds upstream of the flames were made for both reference methane/air flames and acetone vapour/droplet flames, and compared to simulated values of the purely gaseous flames. Spontaneous Raman spectroscopy was used to measure temperature and major species molar fractions across reference methane flames. The results were shown to be in good agreement with the simulations for most of the species, except CO and CO_2, which had too low a signal-to-noise ratio in the product zone. Preliminary measurements of acetone spray/vapour flames showed the capability of the setup to measure Raman signals in the presence of droplets at lowered laser energy. High laser energies led to prompt ignition of the droplets. Potential means of resolving the problem are suggested.

Keywords - laminar flame; counterflow; spray; strained; droplet; premixed; PIV.

Introduction

Two-phase spray combustion plays an important role in industrial processes, energy production and storage, as well as aeronautical and automotive transportation. Injection of fuel via sprays is actively used in internal combustion engines, gas turbines and power generators. The interaction of liquid and gaseous-phase fuels is complex; models typically involve the solution of Eulerian gas phase equations overlaid with Lagrangian solutions for droplets. Recent studies [1, 2] suggested that the effect of droplets could be taken into account directly by parameterizing the effect of their presence on the burning rate. Previous experimental studies on the role of droplets on the burning rate of vaporized mixtures were performed in closed combustion chambers on spherically expanding flames [3, 4]. These suggested that heat release rates were maximum for a particular droplet size, which also varied with the equivalence ratio. A number of computational studies have considered the role of droplets on laminar premixed and diffusion flames, which also revealed a similar behaviour [5, 6]. The transient nature of spherically propagating flames does not lend itself to detailed measurements to provide evidence for such behaviour.

The present study provides a platform for steady measurements of velocities, temperatures and species on the structure of strained laminar flames with added droplets, using measured droplet sizes and liquid fraction concentrations.

The present study is based on initial work by McGrath et al. [7] using the same configuration of acetone/air mixtures to examine the effect of the presence of droplets on flame propagation, compared to an analogous vapour-only mixture. The reference flame speeds at various equivalence ratios were determined as a function of strain rate for droplet-laden spray and vaporized acetone/air laminar premixed flames using particle image velocimetry (PIV). Droplet size and count statistics were obtained using Phase Doppler Particle Anemometry (PDPA), which also yielded the estimated fuel liquid fraction. The study has shown that under lean conditions, incomplete fuel vaporization resulted in leaner vapor-phase equivalence ratios, resulting in lower reference laminar flame speeds. In the case of richer mixtures, large enough droplets were able to cross the flame fronts leading to a fuel surplus in the opposite vapor flame, leading to a reduction in its adiabatic flame temperature and a richer product or reactant zone. One of the limitations of the study was a lack of temperature control of the inlet mixtures. Due to the co-axial vertical arrangement of the burners, the exhaust gases led to transient heating of the top burner, influencing the rate of droplet evaporation and overall flame speed.

The present study builds on that prior work, and incorporates much finer temperature control for both top and bottom flames, allowing for much longer and well-characterised detailed measurements.

This study reports on the results of work in progress for these measurements, including (a) PIV measurements for the modified acetone-vapour-droplet system and (b) preliminary Raman measurements of opposed methane-air flames, in preparation for Raman measurements of acetone flames.

*Corresponding author: maxim.kuvshinov@coria.fr

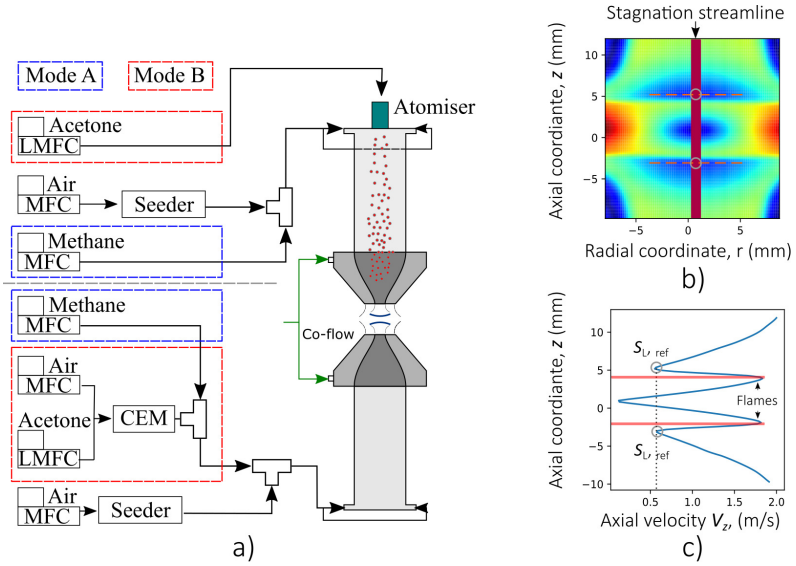

Fig. 1. a) Configuration of the burners and flow delivery for two modes. Mode A (blue) methane/methane gas flames, mode B (red) acetone spray/vapour flames. b) Sample velocity magnitude flow-field with the extraction of the axial velocity profile along the stagnation streamline shown in c).

Experimental methods

Experimental setup

Fig. 1 shows the experimental setup for the twin counterflow burner configuration. The burner nozzles converge the flows from the diameter of 71 mm to 14 cm over a distance of 68 mm to provide a top-hat velocity profile at the exit. The distance between outlets was set to 24 mm (L/D_n = 1.7). Each nozzle is surrounded by a 10 mm wide circular annulus through which a co-flow of nitrogen is delivered to quench the flames and suppress perturbations from the surrounding environment. The top nozzle is surrounded by a stainless steel water-cooling jacket to ensure thermal stability. Thermocouples (RS-pro, type K $\pm$ 1.5 °C) were placed 30 mm from the nozzle exits to measure the fluid temperatures.

The burners were operated in two modes, A and B, producing either pure gas methane flames or acetone spray/vapour flames respectively. In mode A both burners had equivalent fluid delivery systems. Air flow was supplied by a mass flow controller (MFC) (Bronkhorst, F-202AV-M10) into a fluidised bed seeder for particle image velocimetry. Methane was added into the seeded flow and metered by an MFC (Bronkhorst, F-201CV-20K) in order to provide a premixed air/methane mixture at ambient conditions. Nitrogen was used as a sheath flow, supplied by MFCs (Bronkhorst, F-202AV-M10).

The fluid delivery systems in mode B were different top and bottom. The bottom burner was used to produce a vapour flame. Acetone vapour was generated using a controlled evaporation mixing chamber (CEM)(Bronkhorst, W-303A). Liquid acetone was delivered from a pressurised vessel and monitored by a Coriolis mass flow controller (Bronkhorst, M13) into the CEM, which was set to above acetone evaporation temperature of 60 °C. An airflow of 5 SLPM was delivered by an MFC (Bronkhorst, F-201CV-20K) into the air inlet of CEM in order to carry the generated vapor. The vapor-containing flow was then mixed with the seeded flow, as described in mode A. The top burner was used to produce an acetone spray flame. An ultrasonic atomiser (Sono-Tek, 8700-120) was used to create a dilute acetone spray, injected at the inlet of the mixing chamber, 275 mm away from the nozzle exit. A Coriolis mass flow controller (Bronkhorst, M13) with a pump (Tuthill, DGS.19) delivered the liquid acetone to the atomiser. A separate airflow was passed through the second fluidized bed seeder by an MFC (Bronkhorst). Particle-seeded flow was injected into the mixing chamber 25 mm downstream from the atomizer outlet, resulting in an acetone and particle droplet-laden air mixture, with droplet Sauter mean diameter range of 65-75 μm and Stokes number range of 0.500-2.477, increasing with increasing strain rate [7].

Operating conditions

The mixture compositions were defined by the nominal equivalence ratio, ϕ, based on the ratio of injected mass flow rates of fuel and air. For mode A, ϕ = [0.8, 1.0, 1.2]. For mode B, ϕ = [0.75, 0.84, 0.93, 1.02, 1.12, 1.21, 1.3]. For each nominal equivalence ratio, measurements were made for fluid exit velocities, v_{ex} = [1.52-2.60 m/s] in increments of 0.21 m/s for mode A and v_{ex} = [1.62-2.77 m/s] in increments of 0.32 m/s for mode B. This resulted in the range of strain rates K = 250-550 s^{-1} away from flame extinction or nozzle rim attachment.

Gas phase velocity measurements

The velocity fields were determined using PIV. The tracer particle illumination was provided by a double-pulsed Photonics Industries DM60-532 DH laser at the

rate of 4 kHz, and 0.7 W of power per laser head. The beam was shaped into a 1×24 mm^2 sheet. Images were captured by a Phantom v2012 CCD camera, with a 1280 x 800 sensor array, operating in double frame mode at 4 kHz. The camera's field of view was focused by a model K2 Distamax objective. A narrow 532 nm bandpass filter was attached to the objective to reduce background emission. The pixel resolution was 22.7 μm per pixel as calibrated by the target plate. The resultant field of view was set to 17.9×28.9 mm^2. Zirconium powder with an additive of silica oxide (3% by weight) was used to generate gas phase PIV tracer particles (5 μm) with a Stokes number below 0.18. The time interval between the two laser pulses was varied between 54-100 μs, decreasing with increasing flow rates, in order to obtain optimum spatial resolution. A series of 1000 images were collected for every flow rate and equivalence ratio condition for statistical convergence. The images were processed by Davis 10.2.1 using a multipass cross-correlation algorithm. Velocity vector fields were calculated by 3 time pass 16×16 px^2 interrogation window with a 50% overlap, resulting in vector spacing of 180 μm and interrogation region of 360 μm.

The methods developed in [8, 9] were employed in this study for the determination of reference flame speed and strain rates. First, a stagnation streamline was determined, as the streamline along which the radial velocity is zero. The two minimum axial velocities observed upstream of the acceleration produced by each flame were set as the reference flame speeds $S_{\mathrm{L,ref}}$ for the top and bottom flame respectively. The respective strain rates were then determined from the gradient of radial velocities, a, via relation $K = 2a$ at the location of the $S_{\mathrm{L,ref}}$.

Gas phase temperature and mixture composition measurements

Measurements of temperature and gas composition were performed by spontaneous Raman Scattering spectroscopy (SRS). To overcome the weak efficiency of SRS, the molecular excitation was provided by a Nd:YAG (Agilite Continuum) operating at 10 Hz. The laser output was 1.5 J with a top-hat pulse profile and duration of 1 μs. The beam was focused by a f = 1000 mm focal length lens resulting in a beam waist of 200 μm (1/e^2) at focus. The isotropically generated Raman and Rayleigh scattered emission signals were collected at 90°by two telescopes. The first telescope collimated the emission via 100 mm diameter, f = 150 mm achromat lens, which was then focused onto a slit by a f = 300 mm, 100 mm lens, resulting in a probe volume length of 3.2 mm. Rayleigh emission was suppressed by a notch filter (NF03-532E, Semrock, OD = 6, at 532nm, FWHM = 17 nm) placed in the collimation part of the secondary telescope, consisting of two 2-inch, f = 200 and f = 250 lenses respectively. A periscope was then used to rotate the emission from the horizontal beam parallel to the vertical entrance slit of the spectrograph. The single-shot SRS spectra were acquired with the IsoPlane SCT 320 spectrograph (Princeton Instruments) which had a grating of 600 grooves/mm, resulting in spectral resolution of 0.67 nm [10].

The detector camera used was a full-frame back-illuminated CCD (Pixis 400b, Princeton Instruments) with a 1340×400 sensor array and pixel size of 20 μm. A series of 500 images at 3.3 Hz were collected to reach statistical convergence.

The collection was gated by fast electro-optical shutter made-up of Pockels Cells (PCS) to reduce the contribution of flame emission to the background. The PCS were positioned in the collimated part of the second telescope. The gating time for the PCS was set to 1 μs to overlap with the duration of the laser pulse, minimising the camera's exposure to flame emission. An achromatic half-wave plate (AHWP10M-600, Thorlabs) was placed in front of the spectrograph and oriented to maximise its efficiency.

Results

Gas phase velocity measurements

Fig. 2 shows the reference laminar flame speed as a function of strain rate for ϕ = [0.8, 1.0, 1.2], methane gas flames (mode A). Dark grey and white circles represent the single frame and mean values for the top flame, while light grey and white squares represent the single frame and mean values for the bottom flame. The means are grouped by the v_{ex} conditions. Black lines represent the numerical values obtained with Cantera one-dimensional model, using GRI 3.0 mechanism. The values for the top flame are predominantly above the data for the bottom flame, since the mixture temperature at the exit of the top burner is 6 ± 0.81 °C higher than at the exit of the bottom burner as a consequence of heat transfer to the burner's body from the product gases. The velocity gradients for all of the conditions are similar, indicating that the temperature difference is the underlying cause of the value discrepancies. The simulations were performed for the measured inlet mixture temperature of the bottom burner. There is a good agreement between the model and the experimental results for lean and stoichiometric conditions, with the rich condition showing a sharper gradient increase with strain rate. The use of high-speed PIV allowed the detection of periodic synchronised anti-phase oscillation of the two flame fronts at 130 Hz, which becomes more apparent and higher strain rate conditions. Its effects are clearly observed in the ϕ = 1.0 condition, where starting from 400 s^1 the spread of data from the mean dramatically increases. The same behaviour is observed in ϕ = 1.2. These oscillations are undesirable, and their origin is currently being investigated.

Fig. 3 shows the reference laminar flame speed as a function of strain rate for ϕ = [0.83, 1.02, 1.21], acetone spray/vapour flames (mode B). The data is represented in the same fashion as in Fig. 2. Black lines represent the numerical values obtained with Cantera one dimensional model at 28 °C, using mechanism of Pichon et al.

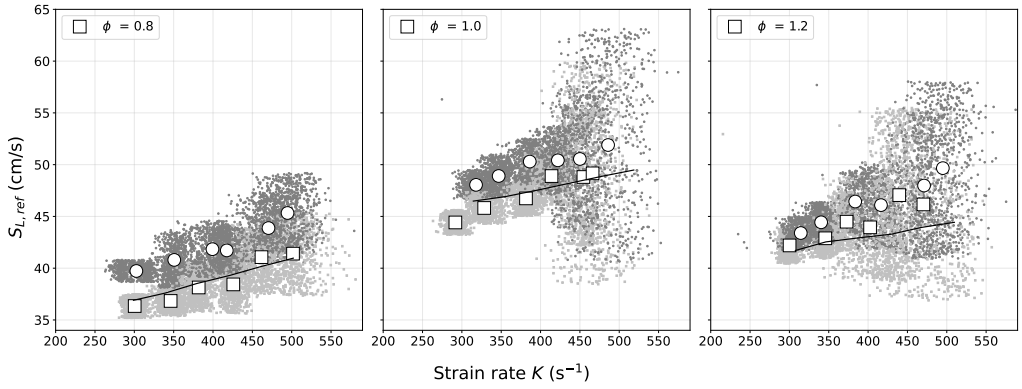

Fig. 2. Reference laminar flame speed $S_{\mathrm{L,ref}}$ as a function of strain rate K for methane gas flames (mode A). Dark grey and light grey points correspond to single measurements of the top and bottom burners respectively. Circles and squares represent average values for top and bottom flames grouped by the v_{ex}. Black lines correspond to Cantera simulations.

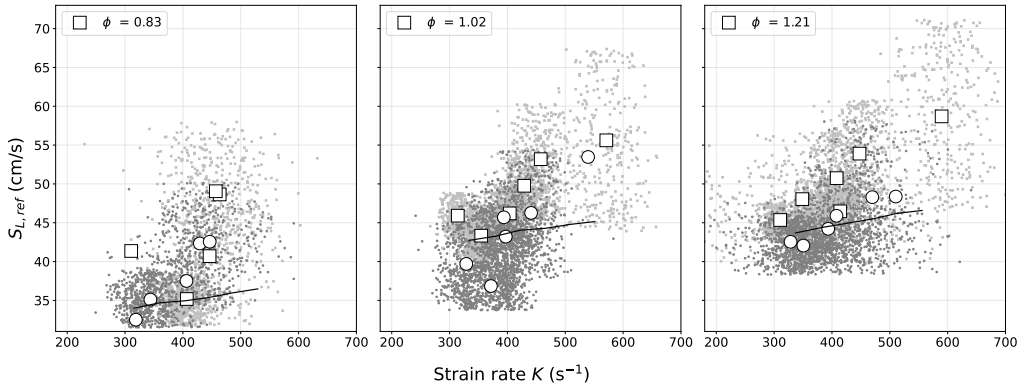

Fig. 3. Reference laminar flame speed $S_{\mathrm{L,ref}}$ as a function of strain rate K for acetone spray/vapour flame (mode B). Dark grey and light grey points correspond to single measurements of the top and bottom burners respectively. Circles and squares represent mean values for top and bottom flames grouped by the v_{ex}. Black lines correspond to Cantera simulations computed using mechanism of Pichon et al.[11]

[11]. Here, the effect of the oscillation in flame fronts is much more apparent, with $S_{\mathrm{L,ref}}$ varying by more than 20 m/s. This is 4 times higher than the variation presented in the original study [7]. Moreover, the disagreement between the experimental and numerical data is assumed to be caused by the oscillation of flame fronts. However, different phenomena compared to mode A can be observed. All of the conditions demonstrate that on average the reference flame speed is lower for the top flame than for the bottom flame. This may be due to incomplete vaporization of the droplets, which makes the inlet mixture both leaner and colder, reducing the effective equivalence ratio and resulting in lower reaction rates. The temperature of the vapour mixture at the exit of the bottom nozzle was measured as 28.5±3°C throughout all the measurements. However, the temperature of the spray mixture at the exit of the top nozzle varied between 8.7-14.1 °C, with colder temperatures present for the richer conditions. Condition ϕ = 1.21 shows the largest disagreement between the two flames. This condition represents the largest temperature difference between the two mixtures. Incomplete vaporization of droplets in the top flame under rich conditions leads to a leaner flame, and an increase in the reference velocity. The droplets from the top flame may also be traversing across the two flame fronts [7], delivering additional fuel to the bottom mixture, in turn making it richer and colder, thus reducing the reference flame speed. However, the contrary is observed, with the reference velocities for the top flame being lower than for the bottom. In order to determine the dominant effect for this discrepancy, PDPA measurements are planned to calculate the liquid fraction of acetone in the mixture, allowing to obtain the effective equivalence ratio and track the droplet population distribution throughout the flame fronts.

Results of gas phase thermometry and species composition

Preliminary measurements using SRS were used to determine the temperature and species composition in reactant and product zones of the counterflow methane flames (mode A). Measurements were performed at nozzle exit velocities of 1.73, 2.17 and 2.60 m/s for the equivalence ratios of 0.8, 1.0 and 1.2. The tempera-

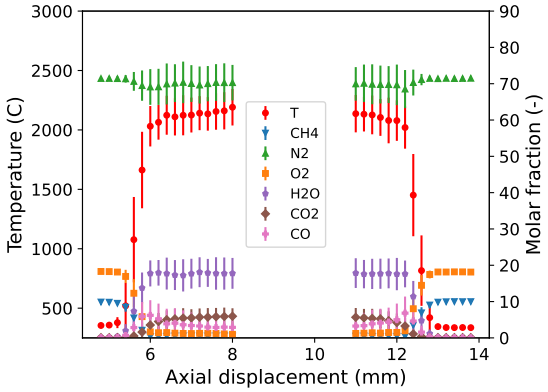

Fig. 4. Axial temperature and species molar fraction concentration measurements for $\phi = 1.0$, $v_{ex} = 2.17$ m/s ($K \approx 440 s^{-1}$), counterflow methane flames.

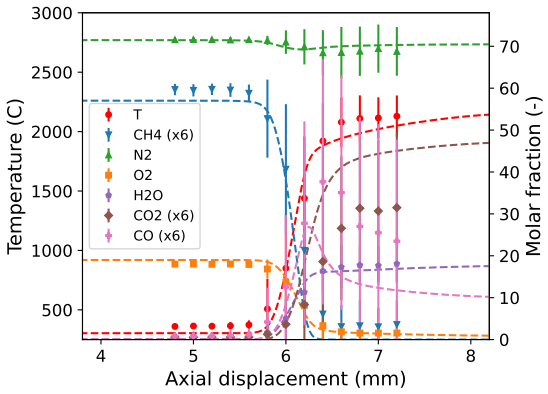

Fig. 5. Axial temperature and species molar fraction concentration measurements (symbols) for ϕ = 1.0, v_{ex} = 2.17 m/s ($K \approx 440 s^{-1}$) counterflow top methane flame. CH_4, CO_2 and CO values were magnified 6 times. Dashed lines show results of 1D Cantera simulations.

ture and species composition values were determined by least-square fitting of the convolution of theoretical spectra of each species of interest with the instrument functions to the single-shot experimental spectra. Further details of the exact procedure and databases of fitting parameters are available in Ref. [10].

Fig. 4 shows the experimentally determined profiles of temperature and species molar concentrations for ϕ = 1.0 counterflow methane flames at a nozzle velocity of 2.17 m/s. The measurements were extracted from the average of the values acquired by fitting individual single-shot spectra. The values for the top and bottom flames are shown from left to right respectively. It can be seen that the profiles are symmetric, with equal temperature and species molar concentrations as expected. The measurement fluctuations represented by the error bars in the reactants low-temperature zone, are much lower when compared to those in the product gases, as the signal is much stronger in regions of higher gas density.

Fig. 5 shows a zoomed section of profiles for the top flame shown in Fig. 4, along with results of 1-D counter-

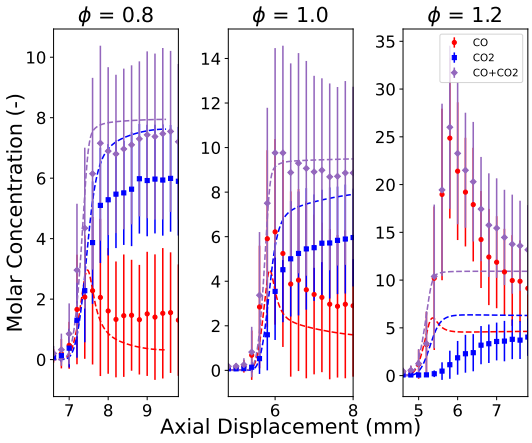

Fig. 6. Experimental (symbols) and simulated (dashed lines) molar concentration profiles of CO (red) and CO_2 (blue) and a sum of CO and CO_2 (purple) for counterflow methane flames with v_{ex} = 1.73 m/s ($K \approx 340 - 360$ s^{-1}) for different equivalence ratios.

flow premixed flame Cantera simulations performed using a GRI 3.0 mechanism. The values for temperature, CH_4, N_2, and H_2O are in good agreement with the simulations in both reactant and product regions. However, there is a discrepancy in the shapes of the gradients, with experimental data exhibiting sharper gradients in values than experimental values. The horizontal orientation of the two flames is parallel to that of the excitation beam. It was noticed that the axial position of the flame varied vertically within a 0.9 mm range, leading to a large variation within the high gradient zone.

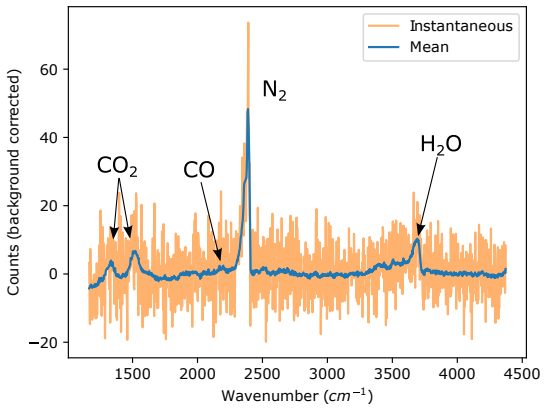

Fig. 7. Mean and instantaneous Raman spectra for a counterflow methane flame at ϕ = 1.0, v_{ex} = 1.73 m/s ($K \approx 360$ s^{-1}) in the product zone.

Very good agreement is found between simulations and measurements of temperature and H_2O molar fractions, but not for CO and CO_2. Fig. 6 shows the experimental and numerical profiles for molar fractions of CO, CO_2 and their sum as a function of equivalence ratio for the inlet fluid velocity of 1.73 m/s ($K \approx 440$ s^{-1}). For the lean and stoichiometric conditions, measured

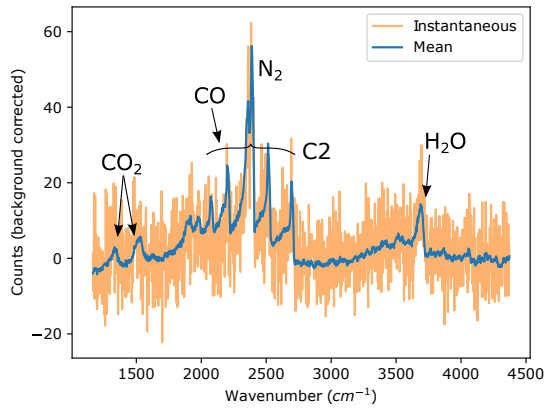

Fig. 8. Mean and instantaneous Raman spectra for a counter-flow methane flame at ϕ = 1.2, v_{ex} = 1.73 m/s ($K \approx 347$ s^{-1}) in the product zone.

CO molar fractions are higher and of CO_2 lower than expected from theory. The signal strengths of CO and CO_2 are very weak in the product zone, as shown in Figs. 7-8, leading to a high measurement uncertainty. The spectral region for CO_2 Raman signal has a high background, and the CO peak is further complicated by its overlap with the rotational Raman emission of N_2 at high temperatures. Finally, in the rich condition, (ϕ = 1.2), the presence of strong C2 Swan band emission leads to significant overlap with the CO signal, resulting in divergence from the expected equilibrium molar fractions of around 25 %.

The SRS method was then applied for preliminary measurements on an acetone spray/methane gas flame, ϕ = 1.0, v_{ex} = 1.73 m/s, for the top and bottom burner respectively. The top burner was run in mode B while the bottom burner was run in mode A. At full laser energy of 1.5 J, frequent and violent optical breakdown events were observed when a droplet passed through the beam volume, as shown in Fig. 9. Shockwaves from the event were sufficiently strong to extinguish the flame or to cause ignition of the gaseous mixture. It was found that such events did not occur at energies below 0.5 J, which was set as the laser energy from then on.

Fig. 10 shows two single instantaneous spectra of acetone spray flame, ϕ = 1.0, v_{ex} = 1.73 m/s ($K \approx 347$ s^{-1}), 4 mm from the spray nozzle exit, in the reactant zone, separated in time by 3 seconds. Expected signals of N_2 and O_2 are observed, along with the stretching mode CH_3 of acetone at 2750 cm^{-1}. For the majority of 500 spectra in the series, the magnitude of CH_3 mode remained lower than that of the N_2, indicating that it comes from the acetone vapor that was created by the droplet evaporation. Sudden spikes of the CH_3 emission, along with unknown mode at 3596 cm^{-1} are observed, as shown in Fig. 11 which arise from the droplets crossing the beam. The magnitude of these modes varies significantly with time. The large magnitude of the CH_3 peak may be linked to a sudden increase of acetone molecular density in a droplet, resulting in liquid phase

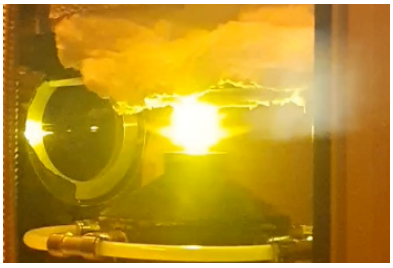

Fig. 9. Optical breakdown of droplets in an acetone spray/methane gas flame, ϕ = 1.0, v_{ex} = 1.73 m/s ($K \approx 347$ s^{-1}).

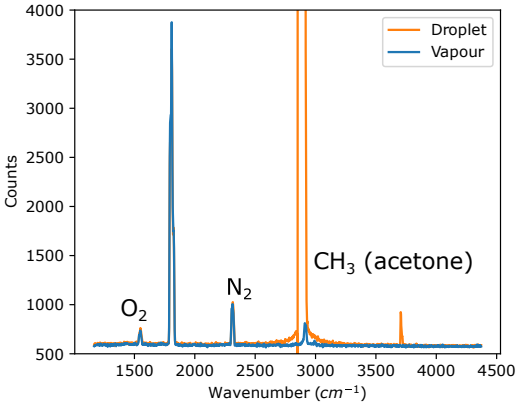

Fig. 10. Single spectrum of acetone spray/ methane gas flame, ϕ = 1.0, v_{ex} = 1.73 m/s ($K \approx 347$ s^{-1}), 4 mm from the spray nozzle exit, reactant zone.

Raman, or laser-induced droplet evaporation, leading to locally high concentrations. Another strong mode is observed at 1711 cm^{-1}, which also varies in magnitude but independent of the CH_3 mode, as shown in Fig. 11. Its origin is currently being investigated.

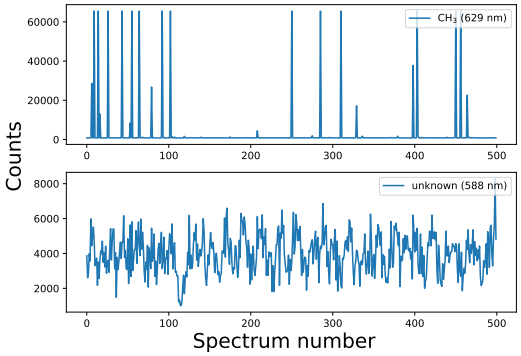

Fig. 11. Variation of CH_3 (top) and unknown modes (588 nm) (bottom) during a series of spectra for acetone spray/methane gas flame, ϕ = 1.0, v_{ex} = 1.73 m/s ($K \approx 347$ s^{-1}), 4 mm from the spray nozzle exit, reactant zone.

Fig. 12 shows an average of 500 spectra of the acetone spray/ methane gas flame, ϕ = 1.0, v_{ex} = 1.73 m/s ($K \approx 347$ s^{-1}), 12 mm from the spray nozzle exit, prod-

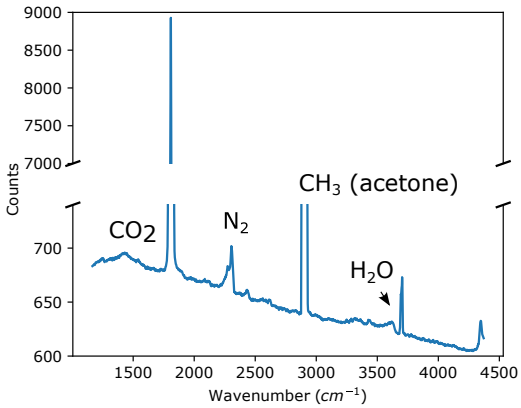

Fig. 12. Averaged spectrum of acetone spray/ methane gas flame, ϕ = 1.0, v_{ex} = 1.73 m/s, 12 mm from the spray nozzle exit, product zone.

uct zone. The acetone spray and methane flames were generated by the top and bottom burner respectively. The CO_2, H_2O and N_2 modes are present, as expected from the product zone. However, a presence of a strong CH_3 mode is still observed, suggesting that droplets continue to pass through the flame front and produce strong Raman signal emission, which contributes to the averaged spectra. The emission at 3600 cm^{-1} is present only in the presence of CH_3 mode. It should be noted that the emission at 1711 cm^{-1}, previously observed in the reactants zone, triples in magnitude, in contrast to a nearly 7 times reduction in gas density.

Conclusions

The effect of fuel droplets on the burning velocity of strained laminar premixed flames was investigated experimentally using optical diagnostics. The twin counterflow burner configuration was used to create premixed acetone vapour flames with the addition of fuel droplets.

Particle image velocimetry (PIV) was used to measure 2D velocities for nominal equivalence ratios in the range (0.8–1.21) as a function of strain rate (250–550 s^{-1}). Measurements of reference flame speeds upstream of the flames were made for both reference methane/air flames and acetone vapour/droplet flames, and compared to simulated values of the purely gaseous flames. Experimental values of the methane/air flame were in agreement with simulated data for the bottom flame. The values for the top flame had the same gradient but were vertically offset as the top mixture temperature was higher due to heating transfer from the exhaust gases to the burner. The measurements of the acetone spray/vapour flame have shown an inverse relation. The latent heat of droplet evaporation significantly reduced the mixture temperature of the top flame compared to the bottom, resulting in lower reference velocity values, respectively. The discrepancy in the reference velocity values of the two flames grew with an increased nominal equivalence ratio due to a higher fraction of liquid droplets. Spontaneous Raman spectroscopy was used to measure temperature and species molar fractions across reference methane flames. The molar fraction and temperature results were shown to be in good agreement with the simulations for most of the species, except CO and CO_2, which had too low a signal-to-noise ratio in the product zone. Preliminary measurements of acetone spray flame showed the capability of the setup to measure Raman signals in the presence of droplets at lowered laser energy. High laser energies led to prompt ignition of the droplets. Two types of spectra were detected, reactants with acetone vapour and reactants with an Acetone droplet crossing the probe volume. Expected products were detected past the flame front along along with strong acetone emission, showing the capability of droplets to cross the flame front.

Acknowledgements

Financial support from the Région Normandie under the Chaire d'Excellence DOLFIN (DrOplet-Laden Flame INteraction) is gratefully acknowledged.

References

[1] A. Vié, B. Franzelli, Y. Gao, T. Lu, H. Wang, and M. Ihme, *Proceedings of the Combustion Institute* **35**, 1675 (2015).

[2] W. Xie, W. Wu, Z. Ren, H. Liu, and M. Ihme, *Physics of Fluids* **33**, 065115 (2021).

[3] S. HAYASHI, S. KUMAGAI, and T. SAKAI, *Combustion Science and Technology* **15**, 169 (1977), ISSN 0010-2202.

[4] H. Nomura, M. Koyama, H. Miyamoto, Y. Ujiie, J. Sato, M. Kono, and S. Yoda, *Proceedings of the Combustion Institute* **28**, 999 (2000), ISSN 1540-7489.

[5] A. Neophytou and E. Mastorakos, *Combustion and Flame* **156**, 1627 (2009), ISSN 0010-2180.

[6] G. Continillo and W. A. Sirignano, *Combustion and Flame* **81**, 325 (1990), ISSN 0010-2180.

[7] D. McGrath, L. Fan, S. Gkantonas, and S. Hochgreb, *Proceedings of the Combustion Institute* **000**, 1 (2022), ISSN 15407489.

[8] C. K. Law, D. L. Zhu, and G. Yu, *Symposium (International) on Combustion* **21**, 1419 (1988), ISSN 0082-0784.

[9] D. L. Zhu, F. N. Egolfopoulos, and C. K. Law, *Symposium (International) on Combustion* **22**, 1537 (1989), ISSN 0082-0784.

[10] F. Guichard, N. Valdez, P. Boubert, D. Honoré, C. Lacour, B. Lecordier, and A. Cessou (2019), Proceedings of the European Combustion Meeting 2019.

[11] S. Pichon, G. Black, N. Chaumeix, M. Yahyaoui, J. M. Simmie, H. J. Curran, and R. Donohue, *Combustion and Flame* **156**, 494 (2009), ISSN 0010-2180.